Electric field induced out-of-plane second-order optical nonlinearity in monolayer transition metal dichalcogenides

Zhizi Guan [1], Yunkun Xu,[2] Junwen Li,[3] Hailong Wang,[4] Zhiwei Peng,[2] Dangyuan Lei,[2,*] and David J. Srolovitz [1,†]

[1]*Department of Mechanical Engineering, The University of Hong Kong, Pokfulam Road, Hong Kong SAR, China*
[2]*Department of Materials Science and Engineering, City University of Hong Kong, Hong Kong SAR, China*
[3]*DFTWorks LLC, Oakton, Virginia 22124, USA*
[4]*CAS Key Laboratory of Mechanical Behavior and Design of Materials, Department of Modern Mechanics, University of Science and Technology of China, Hefei, Anhui 230027, China*

(Received 23 August 2023; revised 24 November 2023; accepted 22 January 2024; published 15 February 2024)

Second-order nonlinear optical effects in monolayer transition-metal dichalcogenides (ML TMDCs) have attracted significant attention; these are almost exclusively associated with their in-plane second-order nonlinear susceptibility arising from the intrinsically broken in-plane inversion symmetry. However, a key challenge is the induction and manipulation of out-of-plane symmetry breaking that governs out-of-plane polarized second-order nonlinear processes such as second-harmonic generation in ML TMDCs. Using first-principle density functional theory, we show that applying an electrostatic field perpendicular to the monolayer plane can induce out-of-plane second-order nonlinear susceptibility ($\chi_{zxx} = \chi_{zyy}$) in the visible wavelength range in the four most representative TMDCs (MoS_2, $MoSe_2$, WS_2, WSe_2), with magnitude comparable to their intrinsic in-plane components (χ_{yyy}). The susceptibility peak values (χ^*_{zxx}, χ^*_{yyy}), with incident energy around half of the C exciton energy in each material, exhibit a linear dependence on the applied field strength E. This behavior originates from the joint effects of field-induced asymmetric out-of-plane charge density distribution and structural deformation. Although the asymmetric charge distribution predominantly governs this effect, the structural deformation also contributes to the overall response in all four ML TMDCs. To accurately describe and predict the induced out-of-plane nonlinear susceptibility in ML TMDCs under varied E, we introduce a structural deformation descriptor τ which exhibits a linear correlation with χ^*_{zxx} to measure the magnitude of the electric-field-induced out-of-plane dipole moment. Our study provides an easy-to-implement approach for generating and tuning the out-of-plane second-order optical nonlinearity in ML TMDCs and hence opens a different avenue for investigating active control of their second-order nonlinear optical processes.

DOI: 10.1103/PhysRevB.109.075417

I. INTRODUCTION

Monolayer transition-metal dichalcogenides (ML TMDCs), consisting of a transition-metal atomic layer sandwiched between two chalcogen atomic layers, have emerged as a promising class of materials for advanced photonics, optoelectronics, and electronics [1–6]. These two-dimensional materials can exhibit highly efficient light-matter interactions through their integration with external photonic structures or their intrinsic polaritonic resonances, giving rise to exceptional linear and nonlinear optical properties [7–10]. Among them, ML MoS_2, $MoSe_2$, WS_2, and WSe_2 are direct-band-gap semiconductors, serving as versatile platforms for second-harmonic generation (SHG), an important nonlinear optical phenomenon that converts two photons of equal frequency into a single photon with double the input photon frequency [11,12]. The extraordinary SHG response arises from the absence of in-plane centrosymmetry in these ML TMDCs; their bulk counterparts are centrosymmetric and exhibit no SHG response.

The SHG response of materials in different directions is strongly influenced by their intrinsic crystalline symmetry, characterized by a third-rank susceptibility tensor $\boldsymbol{\chi}^{(2)}$. ML TMDCs belong to the noncentrosymmetric point group $D_{3h}(\bar{6}m2)$, which implies that $\boldsymbol{\chi}^{(2)}$ has only one nonzero component, denoted χ_{yyy} (where the monolayer lies in the $x-y$ plane, and z is the out-of-plane direction). Consequently, these materials can only convert incident pump light into in-plane polarized SHG radiation, which limits their potential applications [13,14]. The ability to control SHG response in different directions has proven to be crucial in several fields, including second-harmonic microscopy imaging and the generation of some novel lasers [15–17]. Related structures, such as Janus ML TMDCs with an intrinsic out-of-plane electric dipole, exhibit both in-plane and out-of-plane components with a magnitude ratio of 10 : 1 under a 1080 nm pump [18,19]. However, these Janus monolayers cannot be easily obtained by cleavage (like the TMDCs) and their direct synthesis is currently beyond most widely used techniques. Therefore, we explore different approaches for breaking the out-of-plane symmetry in ML TMDCs and achieving SHG tuning. Such

*dangylei@cityu.edu.hk
†srol@hku.hk

advances will be the key to expanding the potential of these materials for photonics and optoelectronics [20,21].

Various approaches have been proposed to manipulate SHG response, including anisotropic strain [22,23], multilayer twisting [24–26], and electrical control [27–31]. Among these approaches, the electrically tunable SHG has been extensively studied since 1967, where an electric field was applied to a nonlinear medium to increase the SHG intensity [32]. Electric field induced second-harmonic generation (EFISH) has been employed in applications in several materials [33–35]. Among two-dimensional (2D) materials and their related structures, the easily fabricated five-atomic-layer-thick In_2Se_3 is a good candidate for EFISH [36,37]. Another example is bilayer graphene, where the out-of-plane symmetry and mid-infrared SHG can be effectively tuned [29,38–40]. In the case of 2D TMDCs, the focus has mainly been on inducing and controlling the in-plane-polarized SHG in bilayers [27,28,41,42]. Meanwhile, the optical properties of 2D TMDCs are strongly influenced by their excitonic states, with A, B, and C excitons at increasing energy levels [43–45]. Achieving resonant SHG entails tuning the incident photon energy to the excitonic transitions. For example, the SHG response of bilayer MoS_2 showed a 60-fold enhancement when the second-harmonic emission energy coincided with the C-exciton resonance (2.5–3.0 eV) [27].

We are aware of only one study, in 2015, that demonstrated tunability of the SHG intensity at the A-exciton resonance in a TMDC (WSe_2 at ≈0.83 eV). The intensity was shown to vary by more than an order of magnitude at low temperature and nearly a factor of four at room temperature through electrostatic doping in a field-effect transistor [31]. However, this report primarily focused on the overall SHG intensity, rather than contributions from the individual components of $\boldsymbol{\chi}^{(2)}$. The limited research on monolayers is associated with the widely accepted notion that perpendicular electric fields have minimal impact on the electronic behavior of ML TMDCs, as supported by theoretical and experimental studies [46–48]. Nevertheless, the SHG response is highly sensitive to symmetry breaking; what causes this sensitivity and the differences between ML TMDCs warrants further investigation.

Here, we present a comprehensive exploration of the induction of out-of-plane SHG susceptibility in four ML TMDCs using perpendicular electrostatic fields with strength E ranging from 0 to 7 V/nm based upon first-principles calculations. Our findings are in agreement with previous experimental observations (peak positions and shapes in Fig. 2. in the absence of an electric field in ML TMDCs). We specifically focus on the influence of the electric field on the components of $\boldsymbol{\chi}^{(2)}$ around the prominent peak (χ^*, which falls within the incident energy range of 1.2 to 1.6 eV), at approximately half the C exciton energy in each material. The peak in the out-of-plane second-order susceptibility χ^*_{zxx} increases linearly with the electric field E, reaching 1.3×10^4 pm^2/V at the largest value of E investigated in this study. The magnitude of χ^*_{zxx} can be attributed to a combination of charge redistribution and structural deformation induced by the electric field; the charge redistribution effect is larger than that associated with structural deformation. We introduce a structure-related descriptor τ, which captures this effect and can be used to predict the E dependence of χ^*_{zxx} in ML TMDCs. Our results provide a solid foundation for future experimental studies and add strong support to the notion that ML TMDCs have significant promise for electrically switchable nonlinear devices.

II. METHODS

We first obtain the optimized crystal structures of ML TMDCs and self-consistent wave functions using ground-state density functional theory (DFT) with the projected augmented wave (PAW) formalism implemented in VASP [49–51]. The electron exchange-correlation interaction is described using the Perdew-Burke-Ernzerhof (PBE) scheme, which is known to underestimate the band gap [52,53]. To overcome this problem and maintain computational efficiency, we employ a scissor correction to correct the band gap according to experimental measurements [54,55] [see details in the Supplemental Material (SM), Sec. I [56]].

In our DFT calculation, we apply an external electric field through imposition of an electric potential gradient perpendicular to the monolayer plane. However, this potential variation can lead to an inconsistency in the charge density of monolayer structures when different out-of-plane vacuum spacings are added to prevent interactions between the planes. This inconsistency arises from electrons spilling into the vacuum region leading to inaccuracies in the second-order susceptibility tensor ($\boldsymbol{\chi}^{(2)}$) calculation [57,58]. We address this issue by limiting the applied electric field to 7 V/nm for a vacuum spacing of 1.5 nm, as described in the SM, Sec. II [56].

III. ELECTRIC-FIELD EFFECTS ON ATOMIC AND ELECTRONIC STRUCTURES

The calculated values of lattice vectors $\boldsymbol{a}$ and $\boldsymbol{b}$ with equal magnitudes denoted as a depicted in Fig. 1(a) for each monolayer are presented in Table S1 of the SM [56], alongside experimental values for comparison. Theoretical and experimental lattice constants exhibit a close agreement, with materials featuring the same chalcogen X displaying similar lattice constants, differing by less than 0.01 nm. In Fig. 1(b), the symbols d_1 and d_2 denote the bond lengths between the metal atom M and the two chalcogen atoms X_1 and X_2, respectively. In the presence of a perpendicular electric field, the field direction will be from X_1 to X_2. These bond lengths are initially equivalent in the pristine layer but vary as the perpendicular electric-field strength E increases. Figure S4 of the SM illustrates the dependence of a, d_1, and d_2 on E for different materials [56]. Notably, the change in a across all monolayers is below 0.25%, while d varies by less than 0.17%. These findings align with previous experimental studies indicating that a perpendicular electric field has a limited impact on the crystal structures of ML TMDCs [46–48]. Additionally, it is worth noting that $MoSe_2$ exhibits the highest rate of electric response for both a and d, while WS_2 exhibits the lowest, suggesting different structural response capabilities to E.

To clearly see the impact of E on charge redistribution, we show the change of out-of-plane charge density $\Delta\rho$ for ML MoS_2 upon application of an electric field $E = 7$ V/nm in Fig. 1(b) as an example. The polarization is clearly reflected within this monolayer; electrons tend to migrate towards

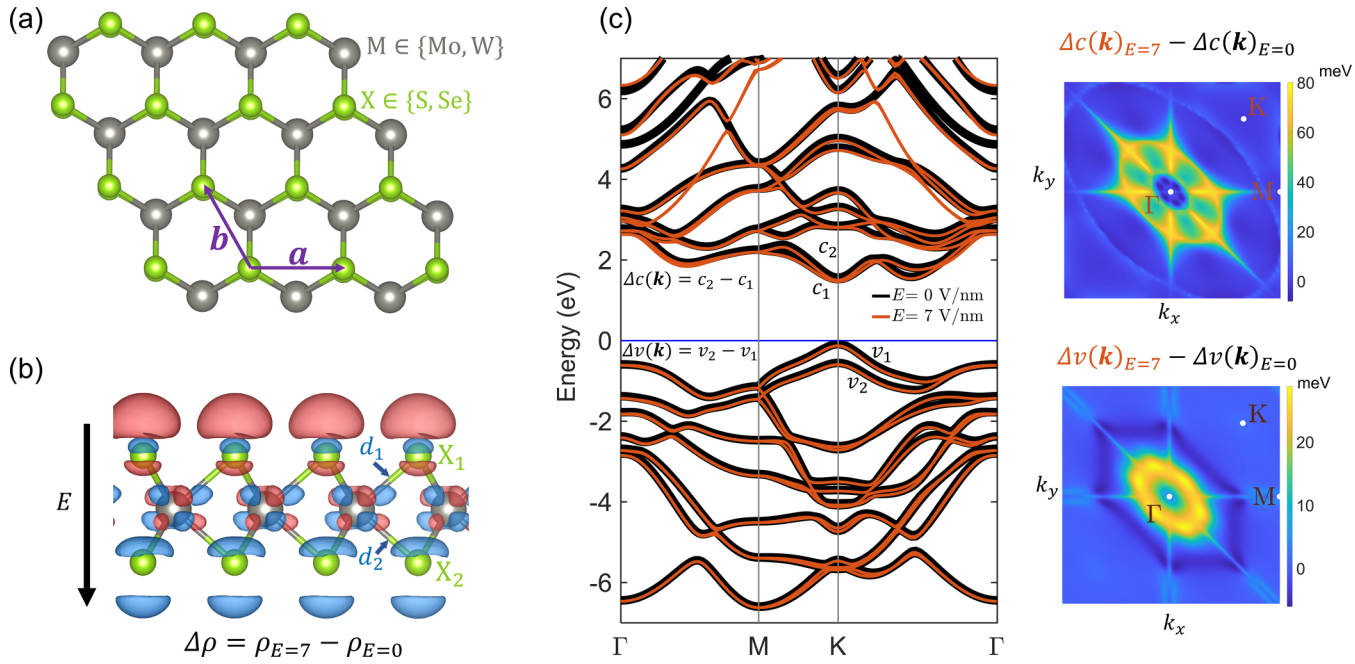

FIG. 1. Crystal structure of four ML TMDCs (MX_2, M ∈{Mo, W}, X ∈{S, Se}) viewed (a) normal and (b) parallel to the TMDCs monolayer plane. In panel (a), we define the unit cell according to lattice vectors $\boldsymbol{a}$, $\boldsymbol{b}$ and, in panel (b), the two inequivalent chalcogen atoms X_i and bond lengths d_i are labeled for a case in which a perpendicular electrostatic field is applied. Panel (b) also shows the valence charge density difference $\Delta\rho$ between MoS_2 with ($E = 7$ V/nm) and without ($E = 0$) an electric field. Red and blue indicate electron accumulation and depletion, respectively. (c) Left: band structure comparison between ML WSe_2 at $E = 0$ (black) and 7 V/nm (red). c_1 and c_2 are the energy distribution on the lower two conduction bands, and v_1 and v_2 label the highest two valence bands. $\Delta c(\boldsymbol{k})$ and $\Delta v(\boldsymbol{k})$ measures the energy splitting between the c and v bands (see Sec. II in the SM and Figs. S1–S3 for a discussion of an artifact in the band structure associated with the large vacuum regions employed [56]). (c) Right: changes in the energy splitting between c_1 and c_2 upon application of an electric field (top) and that between v_1 and v_2 when E is at 0 and 7 V/nm (bottom).

regions with lower electrostatic potential. This leads to charge depletion around X_2 and charge accumulation around X_1. This behavior can be compared with Figs. S2 and S3 of the SM [56], which depict the planar-averaged electrostatic potential energy (PE). This observation provides an explanation for the reduction of bond length d_1 relative to d_2 when an electric field is applied; more electrons are attracted to the vicinity of X_1, resulting in a tighter bond between chalcogen X_1 and M.

Electric fields also affect the band structures, as seen in Figs. 1(c), S5, and S6 [56]. In the absence of an electric field, all four monolayers are direct-band-gap semiconductors (at the K point). After scissor correction to the experimental optical band gap, ML WS_2 and $MoSe_2$ have the largest (1.9 eV) and smallest (1.58 eV) gaps, respectively. While lattice constants are more sensitive to X than M (see Fig. S4 of the SM [56]), the band gap is influenced by both M and (more so) X. When E is increased to 7 V/nm, the band structure undergoes small changes in those localized states near the Fermi level (see SM Sec. II) and all band gaps are slightly reduced (by up to 0.025 eV) [56]. Moreover, as illustrated in Fig. 1(c), electric fields also induce band splitting in the vicinity of the Γ point near the Fermi level. Focusing on the split of the bottom two conduction bands (c_1, c_2) and the top two valence bands (v_1, v_2) in ML WSe_2, as an example (see Fig. S6 of the SM for others [56]), we see a more significant electric field induced splitting in the bottom two conduction bands than in the top two valence bands. The difference in band splitting between $E = 7$ V/nm and $E = 0$ can be up to 80 meV. Electric-field effects in monolayers are smaller than in their corresponding bilayers [47].

IV. THE SECOND-ORDER SUSCEPTIBILITY $\chi^{(2)}$

We first examine the correspondence between our calculated $\boldsymbol{\chi}^{(2)}$ and the experimental SHG response. The experimental SHG signals are commonly measured using a reflection configuration with incident pumped light. Figure 2(a) shows a schematic of the ML TMDC experiment considered here, where a linearly polarized pump light with polarization angle α is incident on the sample at an angle θ with respect to the ML normal. The parallel and perpendicular polarization components of the incident pump field E^{ω} are denoted $E_p^{\omega} = E^{\omega}\cos\alpha$ and $E_s^{\omega} = E^{\omega}\sin\alpha$, respectively. Initially, we consider the case of normal incidence ($\theta = 0$); i.e., the three components of the incident pump electric field are $E_{x'}^{\omega}$, $E_{y'}^{\omega}$, $E_{z'}^{\omega}$.

$$\begin{bmatrix} E_{x'}^{\omega} \\ E_{y'}^{\omega} \\ E_{z'}^{\omega} \end{bmatrix} = \begin{bmatrix} E^{\omega}\cos\alpha \\ E^{\omega}\sin\alpha \\ 0 \end{bmatrix}, \tag{1}$$

where the in-plane components $E_{x'}^{\omega} = E_p^{\omega}$ and $E_{y'}^{\omega} = E_s^{\omega}$ and the out-of-plane component $E_{z'}^{\omega} = 0$. Apart from these two angles, ϕ denotes the azimuthal angle between the crystal ($x - y - z$) and laboratory ($x' - y' - z'$) frames. All DFT results are in the crystal frame (conversion to the laboratory

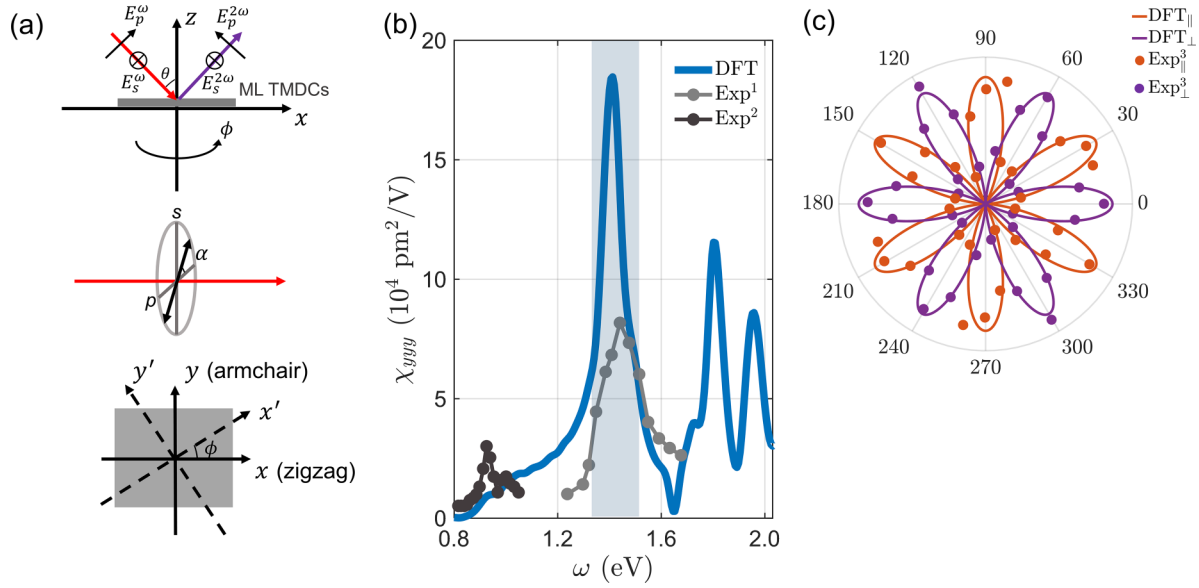

FIG. 2. (a) Top: schematic illustrating the geometry for measuring SHG on ML TMDCs. Middle and bottom: detailed depiction of the polarization (α) and azimuthal (ϕ) angles [the directions in the bottom figure are as per Fig. 1(a)]. (b) Comparison between the DFT results and experiment results (Exp[1] [59] and Exp[2] [60]) as an example for ML MoS_2. The shaded region indicates the peak referred to as χ^*; corresponding to half the C exciton energy. (c) Polar plot depicting the SHG radiation components from ML MoS_2 as a function of the crystal azimuthal angle ϕ. The sixfold pattern is the DFT data according to the proposed Eq. (5) as compared with the experimental data Exp[3] [61].

frame is appropriate for experimental predictions). The ML TMDCs armchair and zigzag directions coincide with the x and y directions.

The SHG polarization components are expressed as

$$P_d(2\omega) = \sum_{e,f} \varepsilon_0 \chi_{\text{def}} E_e^{\omega} E_f^{\omega}, \tag{2}$$

where d, e, f run over x', y', z' in the laboratory frame, ε_0 is the vacuum permittivity, and we focus on the susceptibility tensor components χ_{def} here. The tensor $\boldsymbol{\chi}^{(2)}$ symmetry depends on the crystal symmetry; the electric field affects this symmetry (i.e., the electric field breaks inversion and out-of-plane symmetry). In the absence of an electric field the ML TMDCs have D_{3h} symmetry group, which implies a single, nonzero, independent component, i.e., $-\chi_{yyy} = \chi_{yxx} = \chi_{xyx} = \chi_{xxy}$ (see Fig. S7 of the SM [56]). The E changes the crystal symmetry from D_{3h} to C_{3v}, giving rise to four more independent components $\chi_{xxz} = \chi_{yyz}$, $\chi_{xzx} = \chi_{yzy}$, $\chi_{zxx} = \chi_{zyy}$, and χ_{zzz}. Because the incident energy is fixed, $\chi_{xxz} = \chi_{xzx}$ and $\chi_{yyz} = \chi_{yzy}$. Hence, the $\boldsymbol{\chi}^{(2)}$ for ML TMDCs, subjected to an electric field E only contains four independent components. The coordinates may be written in terms of ϕ as

$$\chi_{\text{def}} = T_{da} T_{eb} T_{fc} \chi_{abc}, \tag{3}$$

where T(ϕ) is a rotation operator

$$T(\phi) = \begin{bmatrix} \cos\phi & \sin\phi & 0 \\ -\sin\phi & \cos\phi & 0 \\ 0 & 0 & 1 \end{bmatrix}, \tag{4}$$

and the polarization is

$$P_{x'y'z'}(2\omega) = \epsilon_0 E^{\omega 2} \begin{pmatrix} \chi_{yyy} \sin(2\alpha + 3\phi) \\ \chi_{yyy} \cos(2\alpha + 3\phi) \\ \chi_{zxx} \end{pmatrix}. \tag{5}$$

Equation (5) shows that, at normal incidence, the in-plane polarization $P_{x'}$ and $P_{y'}$ depend on χ_{yyy} and the polarization and azimuthal angles. On the other hand, the out-of-plane polarization is determined by χ_{zxx} and is independent of angle. Therefore, for the assessment of out-of-plane and in-plane SHG, we need only focus upon two $\boldsymbol{\chi}^{(2)}$ components, χ_{zxx} and χ_{yyy}. In practical experimental designs, the detection of second-harmonic radiation is performed in the parallel ($E_p^{2\omega}$) and perpendicular ($E_s^{2\omega}$) directions (relative to the polarization of the pump field) and the corresponding detected intensities are denoted I_p and I_s. It follows that $I_p \propto (E_p^{2\omega})^2$ and $I_s \propto (E_s^{2\omega})^2$. However, at normal incidence, $E^{2\omega}$ is directly proportional to the in-plane polarization components, i.e., $E_p^{2\omega} \propto P_{x'}(2\omega)$ and $E_s^{2\omega} \propto P_{y'}(2\omega)$. Consequently, no out-of-plane SHG can be detected in such experiments.

To detect out-of-plane polarization, we employ oblique incidence, i.e., $\theta \neq 0$. Under this condition, Eq. (1) becomes

$$\begin{bmatrix} E_{x'}^{\omega} \\ E_{y'}^{\omega} \\ E_{z'}^{\omega} \end{bmatrix} = \begin{bmatrix} E^{\omega} \cos\alpha \cos\theta \\ E^{\omega} \sin\alpha \\ E^{\omega} \cos\alpha \sin\theta \end{bmatrix}. \tag{6}$$

Applying the same methodology, we see that $E^{2\omega}$ is directly proportional to the polarization components involving θ: $E_p^{2\omega} \propto -P_{x'} \cos\theta + P_{z'} \sin\theta$, and $E_s^{2\omega} \propto P_{y'}$. To simplify

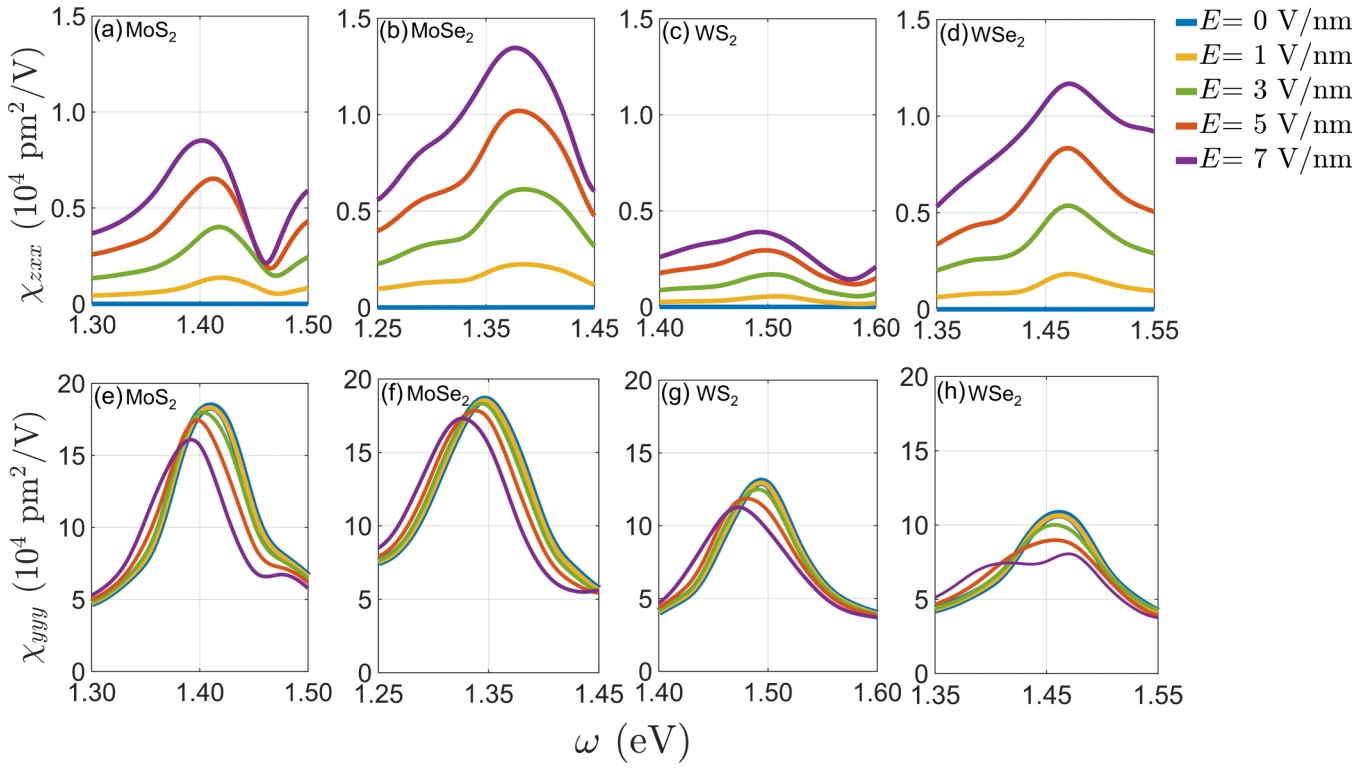

FIG. 3. (a)–(d) Out-of-plane χ_{zxx} and (e)–(h) in-plane χ_{yyy} SHG susceptibility magnitude versus incident photon frequency ω for several electric fields E from 0 to 7 V/nm in the energy range close to half the C exciton energy in different monolayers.

these results and facilitate experimental postprocessing, one may select a specific linear polarization direction $\alpha = 0$. Consequently, the SHG intensities in the two directions become

$$I_p \propto [\chi_{zxx} \sin(\theta) + \chi_{yyy} \sin(3\phi) \cos(\theta)]^2,$$
$$I_s \propto \frac{{\chi_{yyy}}^2 [\cos(6\phi) + 1]}{2}. \quad (7)$$

Equation (7) demonstrates that, under oblique incidence, the two $\boldsymbol{\chi}^{(2)}$ components χ_{zxx} and χ_{yyy} govern the SHG intensity. Thus, we focus on the magnitude of the out-of-plane (χ_{zxx}) and in-plane (χ_{yyy}) SHG susceptibilities.

Figure 2(b) shows the magnitude of χ_{yyy} for ML MoS_2 in the absence of an electric field compared with extant experimental results [59–61]. Here, $\chi_{zxx} = 0$ since there is no electric field induced out-of-plane symmetry breaking. The MoS_2 experimental spectrum exhibits a prominent peak at $\omega \approx 0.85$ eV (slightly higher energy than half of the band gap). This peak arises from band splitting at the K point, albeit with reduced intensities because our current DFT calculations do not include excitonic effects. Previous experiments have demonstrated that the peaks, located near half the A and B exciton energies, are enhanced by excitonic resonances [27,31,59,62].

The most prominent peak in our DFT results appears between 1.3 and 1.5 eV, corresponding to half the energy of the well-known C transition in ML TMDCs [43,63]. We label this peak χ^* [shaded in blue in Fig. 2(b)], since it exhibits the highest sensitivity to an electric field—the main focus of this investigation. However, note that discrepancies in the susceptibility intensity can even arise among different experiments, particularly for 2D materials, because of issues related to the definition of the layer thickness and broadening in the DFT calculations [64]. Figure 2(c) shows a comparison between the DFT in-plane χ_{yyy} as a function of the azimuthal angle ϕ at $\omega = 1.53$ eV with the experimental values. As expected, we observe the same sixfold rotational symmetry pattern according to Eq. (5) when varying ϕ alone. Our calculations provide deep insights into fundamental mechanisms, susceptibility peak positions and shapes, facilitating a comprehensive analysis of the effects induced by electric fields on χ^*.

V. ELECTRIC-FIELD EFFECTS ON OUT-OF-PLANE AND IN-PLANE SECOND-HARMONIC GENERATION SUSCEPTIBILITY

Figure 3 presents the out-of-plane and in-plane SHG susceptibilities $\chi^*_{zxx}(\omega)$ and $\chi^*_{yyy}(\omega)$ for four ML TMDCs for electric fields $0 \leqslant E \leqslant 7$ V/nm. The χ^* peak intensity exhibits vary with E, along with a redshift with increasing field strength. This redshift may be attributed to changes in the band gap and increased band splitting with increasing electric-field strength. MoS_2 and $MoSe_2$ show additional peaks in spectrum when the incident photon energy aligns with the band gap. However, the sensitivity of these peaks to E, in terms of both position and intensity, is relatively small (see Fig. S8 of the SM [56]).

Figure 3 aligns with our initial expectation that an out-of-plane electric field will modify the symmetry group of ML TMDCs, thereby introducing additional nonzero components

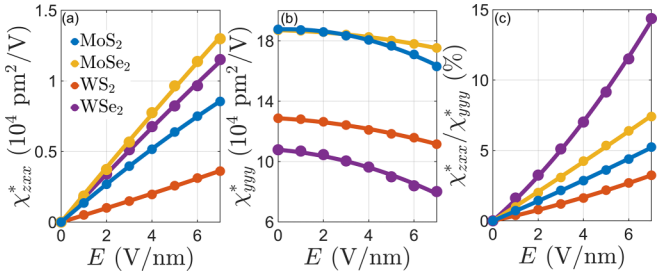

FIG. 4. The variation of the (a) out-of-plane χ^*_{zxx} and (b) in-plane χ^*_{yyy} susceptibility with electric-field strength along with (c) their ratio. The symbols are DFT data and the lines are second-order polynomial fits (see Table S2 of the SM for fitting parameters [56]).

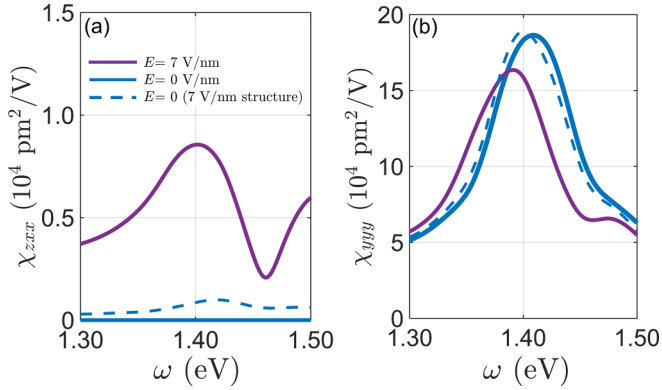

FIG. 5. Panels (a) and (b) show χ_{zxx} and χ_{yyy} versus the incident photon frequency for ML MoS_2. The solid lines represent the data without and with (7 V/nm) an electric field, respectively. The dashed blue line is based on the structure relaxed at $E = 7$ V/nm but with no electric field. This shows the relative importance of structure change and charge redistribution.

to the $\boldsymbol{\chi}^{(2)}$ tensor. Both peaks in a specific material exhibit almost the same position. With increasing E, the out-of-plane χ_{zxx} peaks significantly broaden, the in-plane χ_{zxx} peaks do not. Interestingly, the out-of-plane χ_{zxx} peaks heights increase with increasing E, while the in-plane χ_{zxx} peak heights decrease. This may be seen more clearly in Figs. 4(a) and 4(b), where we plot the peak heights χ^*_{zxx} and χ^*_{yyy} versus the electric-field strength. χ^*_{zxx} increases nearly linearly with E, providing an effective description of the electric field induced out-of-plane symmetry-breaking process (see Fig. S10 of the SM [56]). Among the monolayers, $MoSe_2$ (WS_2) shows the strongest (weakest) effects of the electric field, consistent with the effect of E on the structure (see Sec. III).

Experimentally, it is more convenient to measure the ratio between χ^*_{zxx} and χ^*_{yyy} by calculating the ratio of I_p to I_s, as per Eq. (7). Figure 4(c) shows $\chi^*_{zxx}/\chi^*_{yyy}$ versus the electric-field strength. This ratio also varies (nearly) linearly with E; the effect of the electric field is strongest for WSe_2 (15% at 7 V/nm) and weakest for WS_2 (3% at 7 V/nm). This ratio can be compared with experimental reports on Janus monolayer MoSSe, which show an intrinsic out-of-plane dipole due to different chalcogen species. Their experimental result demonstrates that intensity of the out-of-plane component of $\boldsymbol{\chi}^{(2)}$ is 10% of the in-plane component of $\boldsymbol{\chi}^{(2)}$ at a 1080 nm pump [18]. Our results demonstrate that a similar magnitude out-of-plane component of $\boldsymbol{\chi}^{(2)}$ by application of an electric field in these easy to produce TMDCs (compared with the Janus structure).

To analyze the origin of the effects induced by the perpendicular electric field, we must separate the dominant physical effects of that field; (i) electric field induced deformation of the monolayer structure and (ii) electric field induced charge redistribution. The structural deformation can be described through variations in the bond lengths or atomic layer separations in the ML TMDCs. A gradient in either of these along the monolayer normal breaks the out-of-plane symmetry of the monolayer which, in turn, yields an out-of-plane SHG. We note that applying anisotropic external strains has been shown to be an efficient means of tuning SHG [22,65–72]. The out-of-plane potential difference associated with an electric field also breaks the out-of-plane symmetry; regions of low electric potential attract more electrons while regions of high electric potential become electron depleted [see Fig. 1(b)]. Here we consider and separate these two factors that can induce SHG via a perpendicular electric field. While we focus on ML MoS_2 here, results for the other monolayers are shown in Fig. S9 of the SM [56].

To separate these two effects, we proceed as follows: First, we obtain the relaxed ML atomic structures at $E = 0$ and 7 V/nm and determine χ for both. Second, we take the relaxed structure at $E = 7$ V/nm and, without further atomic relaxation, calculate $\boldsymbol{\chi}^{(2)}$ without an electric field, $E = 0$. This $\boldsymbol{\chi}^{(2)}$ is the second-order susceptibility of the (strained) 7 V/nm structure without the effect of electric field induced charge redistribution. The effect of charge redistribution can then be determined by comparing this result with that for a finite electric field, $E = 7$ V/nm. Figure 5(a) shows that the deformation-induced χ^*_{zxx} component accounts for 12.08% of the absolute peak induced by the 7 V/nm electric field in ML MoS_2 (this is comparable to the effect induced by $E = 1$ V/nm). For ML $MoSe_2$, WS_2, and WSe_2, the effect of the deformation (from the 7 V/nm field) accounts for 12.55%, 5.15%, and 11.98%, respectively. On the other hand, the deformation associated with the 7 V/nm field has very little effect on χ^*_{yyy}; only inducing a slight redshift compared with the undeformed monolayer—see Fig. 5(b). Hence, the primary contribution to the electric field induced second-order susceptibility is associated with charge redistribution. The pure deformation effect can, in practice, be neglected for the in-plane χ^*_{yyy}, but makes a substantial contribution to χ^*_{zxx}. This suggests that the structural deformation component may serve as a reliable descriptor for the out-of-plane χ^*_{zxx}, enabling a unified description across different ML TMDCs.

To quantify the degree of out-of-plane symmetry breaking and establish its relationship with χ^*_{zxx}, we introduce a structural descriptor τ. We define τ based on the schematic plot shown in Fig. 6(a), which depicts two scenarios: $E = 0$ (opaque atoms) and 7 V/nm (translucent atoms). In this analysis, we consider a virtual "center chalcogen atom" that represents the mean position of the chalcogen atoms in two opposite chalcogen layers (while keeping the metal atom stationary). In the structure with no electric field, this center chalcogen atom is coplanar with the metal atoms. However,

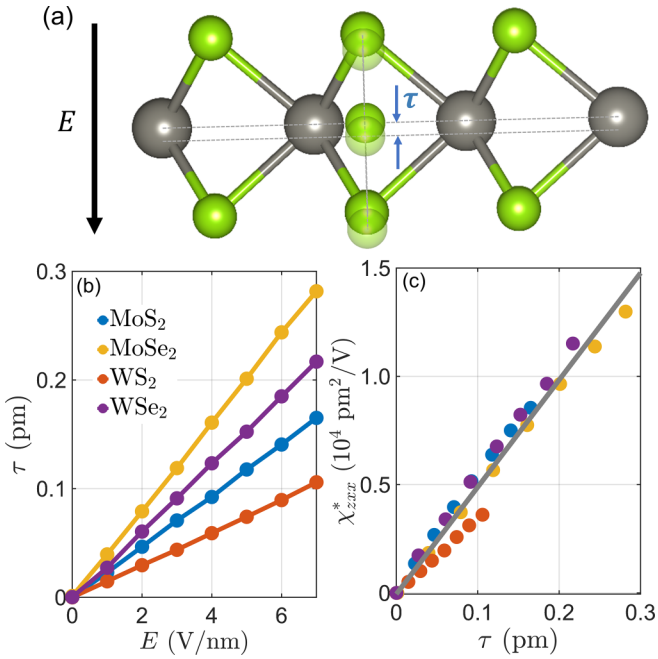

FIG. 6. (a) A schematic plot for defining τ using a virtual "center chalcogen atom" positioned at the out-of-plane structural center of the top and bottom chalcogen planes. The opaque and translucent chalcogen atoms represent relaxed atom positions under $E = 0$ and 7 V/nm, respectively. The shift distance associated with the electric field is labeled τ. (b) The variation of τ with the applied out-of-plane electric-field strength E for all four TMDCs (fitting parameters can be found in Table S2 of the SM [56]). (c) The variation of the out-of-plane χ^*_{zxx} with the structural descriptor τ.

when an electric field is applied, the center chalcogen atom is displaced from the metal plane toward the chalcogen plane where electrons preferentially accumulate [see Fig. 6(a)]; τ measures this shift in the out-of-plane direction. In this sense, τ is a measure of the electric field induced, out-of-plane dipole moment (heuristically assuming the charges on the metal and chalcogens are constant).

As E increases from 0 to 7 V/nm, τ increases in direct proportion [see Fig. 6(b)]. This trend is similar to the variation of χ^*_{zxx} with electric field [Fig. 4(a)]. Since both τ and χ^*_{zxx} scale linearly with E, τ scales linearly with χ^*_{zxx}. Interestingly, since the slopes of τ and χ^*_{zxx} versus E vary between the monolayers in nearly the same manner, a single line describes the relationship between τ and χ^*_{zxx} for all four ML TMDCs. The resulting relationship can be expressed as $\chi^*_{zxx} = 4.942 \times 10^8 \tau$. The introduction of τ as a structural descriptor characterizing out-of-plane SHG in TMDCs has promise for high-throughput computation and machine-learning methodologies for material discovery. By incorporating τ as a computationally efficient screening parameter, DFT calculations can efficiently narrow the search space for and rapidly identify materials that exhibit enhanced second-harmonic generation responses without the need for extensive calculations to determine $\chi^{(2)}$. This accelerated discovery approach is an enabler for novel SHG materials with potential for advanced optoelectronic and photonics applications.

VI. CONCLUSIONS

Our study presents a comprehensive investigation of the application of perpendicular electric fields for enhancing SHG in ML TMDCs. We demonstrate that an electric field induces out-of-plane SHG response in TMDCs and is an effective tuning mechanism for both out-of-plane (χ_{zxx}) and in-plane (χ_{yyy}) SHG susceptibilities. While the influence of E on the atomic and electronic structures of monolayers has been largely overlooked, we demonstrate its significant role in shaping the asymmetric distribution of electrons and band splitting, which in turn affects SHG. By varying E from 0 to 7 V/nm, we observe a linear increase in χ_{zxx} accompanied by a reduction in χ_{yyy} within the energy range of approximately half of the C exciton (the peak value is denoted χ^*). Notably, the out-of-plane susceptibility χ^*_{zxx} is up to 15% the value of the in-plane susceptibility χ^*_{yyy} in the ML WSe_2 for fields up to $E = 7$ V/nm. This is comparable to that previously reported for Janus monolayer MoSSe.

We introduce an innovative approach to disentangle the contributions arising from charge redistribution and structural deformation. Although charge redistribution was shown to dominate deformation in determining the effect of the electric field on the out-of-plane susceptibility, our findings demonstrate the significance of deformation. To further enhance our understanding and predict the behavior of χ_{zxx} under different E, we propose a readily measurable structural descriptor τ, which is related to the out-of-plane polarization. We demonstrate that not only is χ^*_{zxx} directly proportional to τ, but the same relationship applies to all four TMDCs examined here. We expect an external electric field can likewise be used to tune the out-of-plane second-order susceptibility in other 2D semiconductors; e.g., this effect should be easily observed in monolayers of greater thickness—such as phosphorene and In_2Se_3. Overall, our study provides valuable insights into the generation and tunability of out-of-plane second-order nonlinear optical nonlinearity in ML TMDCs, opening up different avenues for exploring active control of their second-order optical processes and potential utilization in optoelectronic and photonic devices.

ACKNOWLEDGMENTS

The authors acknowledge the financial support by the Research Grants Council of Hong Kong (Y.X., Z.P., and D.L. GRF Grant No. 15304519, D.J.S. and Z.G. - GRF Grant No. 11211019), and support from the National Natural Science Foundation of China (H.W. - Grants No. 12172347 and No. 12232016).

[1] B. Radisavljevic, A. Radenovic, J. Brivio, V. Giacometti, and A. Kis, Single-layer MoS_2 transistors, Nat. Nanotechnol. **6**, 147 (2011).

[2] A. Splendiani, L. Sun, Y. Zhang, T. Li, J. Kim, C.-Y. Chim, G. Galli, and F. Wang, Emerging photoluminescence in monolayer MoS_2, Nano Lett. **10**, 1271 (2010).

[3] Q. H. Wang, K. Kalantar-Zadeh, A. Kis, J. N. Coleman, and M. S. Strano, Electronics and optoelectronics of two-dimensional transition metal dichalcogenides, Nat. Nanotechnol. **7**, 699 (2012).

[4] M. Chhowalla, H. S. Shin, G. Eda, L.-J. Li, K. P. Loh, and H. Zhang, The chemistry of two-dimensional layered transition metal dichalcogenide nanosheets, Nat. Chem. **5**, 263 (2013).

[5] Z. Lou, Z. Liang, and G. Shen, Photodetectors based on two dimensional materials, J. Semicond. **37**, 091001 (2016).

[6] C. Xia and J. Li, Recent advances in optoelectronic properties and applications of two-dimensional metal chalcogenides, J. Semicond. **37**, 051001 (2016).

[7] F. Xia, H. Wang, D. Xiao, M. Dubey, and A. Ramasubramaniam, Two-dimensional material nanophotonics, Nat. Photonics **8**, 899 (2014).

[8] M. Stührenberg, B. Munkhbat, D. G. Baranov, J. Cuadra, A. B. Yankovich, T. J. Antosiewicz, E. Olsson, and T. Shegai, Strong light–matter coupling between plasmons in individual gold bi-pyramids and excitons in mono-and multilayer WSe_2, Nano Lett. **18**, 5938 (2018).

[9] H. Chen, V. Corboliou, A. S. Solntsev, D.-Y. Choi, M. A. Vincenti, D. De Ceglia, C. De Angelis, Y. Lu, and D. N. Neshev, Enhanced second-harmonic generation from two-dimensional $MoSe_2$ on a silicon waveguide, Light: Sci. Appl. **6**, e17060 (2017).

[10] J. Xiao, Z. Ye, Y. Wang, H. Zhu, Y. Wang, and X. Zhang, Nonlinear optical selection rule based on valley-exciton locking in monolayer WS_2, Light: Sci. Appl. **4**, e366 (2015).

[11] P. Franken, A. E. Hill, C. E. Peters, and G. Weinreich, Generation of optical harmonics, Phys. Rev. Lett. **7**, 118 (1961).

[12] J. Zhang, W. Zhao, P. Yu, G. Yang, and Z. Liu, Second harmonic generation in 2D layered materials, 2D Mater. **7**, 042002 (2020).

[13] B. T. Fichera, A. Kogar, L. Ye, B. Gökce, A. Zong, J. G. Checkelsky, and N. Gedik, Second harmonic generation as a probe of broken mirror symmetry, Phys. Rev. B **101**, 241106(R) (2020).

[14] J. Dougherty and S. Kurtz, A second harmonic analyzer for the detection of non-centrosymmetry, J. Appl. Crystallogr. **9**, 145 (1976).

[15] X. Yin, Z. Ye, D. A. Chenet, Y. Ye, K. O'Brien, J. C. Hone, and X. Zhang, Edge nonlinear optics on a MoS_2 atomic monolayer, Science **344**, 488 (2014).

[16] J. Butet, J. Duboisset, G. Bachelier, I. Russier-Antoine, E. Benichou, C. Jonin, and P.-F. Brevet, Optical second harmonic generation of single metallic nanoparticles embedded in a homogeneous medium, Nano Lett. **10**, 1717 (2010).

[17] H. Wu, H. Yu, Z. Yang, X. Hou, X. Su, S. Pan, K. R. Poeppelmeier, and J. M. Rondinelli, Designing a deep-ultraviolet nonlinear optical material with a large second harmonic generation response, J. Am. Chem. Soc. **135**, 4215 (2013).

[18] A. Y. Lu, H. Zhu, J. Xiao, C. P. Chuu, Y. Han, M. H. Chiu, C. C. Cheng, C. W. Yang, K. H. Wei, Y. Yang, Y. Wang, D. Sokaras, D. Nordlund, P. Yang, D. A. Muller, M. Y. Chou, X. Zhang, and L. J. Li, Janus monolayers of transition metal dichalcogenides, Nat. Nanotechnol. **12**, 744 (2017).

[19] J. Zhang, S. Jia, I. Kholmanov, L. Dong, D. Er, W. Chen, H. Guo, Z. Jin, V. B. Shenoy, L. Shi, and J. Lou, Janus monolayer transition-metal dichalcogenides, ACS Nano **11**, 8192 (2017).

[20] T. W. Lo, Q. Zhang, M. Qiu, X. Guo, Y. Meng, Y. Zhu, J. J. Xiao, W. Jin, C. W. Leung, and D. Lei, Thermal redistribution of exciton population in monolayer transition metal dichalcogenides probed with plasmon–exciton coupling spectroscopy, ACS Photonics **6**, 411 (2019).

[21] T. W. Lo, X. Chen, Z. Zhang, Q. Zhang, C. W. Leung, A. V. Zayats, and D. Lei, Plasmonic nanocavity induced coupling and boost of dark excitons in monolayer WSe_2 at room temperature, Nano Lett. **22**, 1915 (2022).

[22] C. He, R. Wu, L. Zhu, Y. Huang, W. Du, M. Qi, Y. Zhou, Q. Zhao, and X. Xu, Anisotropic second-harmonic generation induced by reduction of in-plane symmetry in 2D materials with strain engineering, J. Phys. Chem. Lett. **13**, 352 (2022).

[23] L. Mennel, M. Paur, and T. Mueller, Second harmonic generation in strained transition metal dichalcogenide monolayers: MoS_2, $MoSe_2$, WS_2, and WSe_2, APL Photonics **4**, 034404 (2019).

[24] L. Du, Y. Dai, and Z. Sun, Twisting for tunable nonlinear optics, Matter **3**, 987 (2020).

[25] F. Yang, W. Song, F. Meng, F. Luo, S. Lou, S. Lin, Z. Gong, J. Cao, E. S. Barnard, E. Chan, L. Yang, and J. Yao, Tunable second harmonic generation in twisted bilayer graphene, Matter **3**, 1361 (2020).

[26] K. Yao, N. R. Finney, J. Zhang, S. L. Moore, L. Xian, N. Tancogne-Dejean, F. Liu, J. Ardelean, X. Xu, D. Halbertal, K. Watanabe, T. Taniguchi, H. Ochoa, A. Asenjo-Garcia, X. Zhu, D. N. Basov, A. Rubio, C. R. Dean, J. Hone, and P. J. Schuck, Enhanced tunable second harmonic generation from twistable interfaces and vertical superlattices in boron nitride homostructures, Sci. Adv. **7**, eabe8691 (2021).

[27] J. Klein, J. Wierzbowski, A. Steinhoff, M. Florian, M. Rösner, F. Heimbach, K. Müller, F. Jahnke, T. O. Wehling, J. J. Finley, and M. Kaniber, Electric-field switchable second-harmonic generation in bilayer MoS_2 by inversion symmetry breaking, Nano Lett. **17**, 392 (2017).

[28] H. Yu, D. Talukdar, W. Xu, J. B. Khurgin, and Q. Xiong, Charge-induced second-harmonic generation in bilayer WSe_2, Nano Lett. **15**, 5653 (2015).

[29] S. J. Brun and T. G. Pedersen, Intense and tunable second-harmonic generation in biased bilayer graphene, Phys. Rev. B **91**, 205405 (2015).

[30] J. Wang, N. Han, Z. Luo, M. Zhang, X. Chen, Y. Liu, Y. Hao, J. Zhao, and X. Gan, Electrically tunable second harmonic generation in atomically thin ReS_2, ACS Nano **16**, 6404 (2022).

[31] K. L. Seyler, J. R. Schaibley, P. Gong, P. Rivera, A. M. Jones, S. Wu, J. Yan, D. G. Mandrus, W. Yao, and X. Xu, Electrical control of second-harmonic generation in a WSe_2 monolayer transistor, Nat. Nanotechnol. **10**, 407 (2015).

[32] C. Lee, R. Chang, and N. Bloembergen, Nonlinear electroreflectance in silicon and silver, Phys. Rev. Lett. **18**, 167 (1967).

[33] R. Bavli and Y. B. Band, Relationship between second-harmonic generation and electric-field-induced second-harmonic generation, Phys. Rev. A **43**, 507 (1991).

[34] K. Lee, J. Park, B. J. Kang, W. T. Kim, H.-D. Kim, S. Baek, K. J. Ahn, B. Min, and F. Rotermund, Electrically controllable terahertz second-harmonic generation in GaAs, Adv. Opt. Mater. **8**, 2000359 (2020).

[35] A. Widhalm, C. Golla, N. Weber, P. Mackwitz, A. Zrenner, and C. Meier, Electric-field-induced second harmonic generation in silicon dioxide, Opt. Express **30**, 4867 (2022).

[36] W. Ding, J. Zhu, Z. Wang, Y. Gao, D. Xiao, Y. Gu, Z. Zhang, and W. Zhu, Prediction of intrinsic two-dimensional ferroelectrics in In_2Se_3 and other III_2-VI_3 van der Waals materials, Nat. Commun. **8**, 14956 (2017).

[37] Y. Zhou, D. Wu, Y. Zhu, Y. Cho, Q. He, X. Yang, K. Herrera, Z. Chu, Y. Han, M. C. Downer, H. Peng, and K. Lai, Out-of-plane piezoelectricity and ferroelectricity in layered α-In_2Se_3 nanoflakes, Nano Lett. **17**, 5508 (2017).

[38] T. Ohta, A. Bostwick, T. Seyller, K. Horn, and E. Rotenberg, Controlling the electronic structure of bilayer graphene, Science **313**, 951 (2006).

[39] Y. Zhang, T.-T. Tang, C. Girit, Z. Hao, M. C. Martin, A. Zettl, M. F. Crommie, Y. R. Shen, and F. Wang, Direct observation of a widely tunable bandgap in bilayer graphene, Nature (London) **459**, 820 (2009).

[40] S. Wu, L. Mao, A. M. Jones, W. Yao, C. Zhang, and X. Xu, Quantum-enhanced tunable second-order optical nonlinearity in bilayer graphene, Nano Lett. **12**, 2032 (2012).

[41] S. Shree, D. Lagarde, L. Lombez, C. Robert, A. Balocchi, K. Watanabe, T. Taniguchi, X. Marie, I. C. Gerber, M. M. Glazov, L. E. Golub, B. Urbaszek, and I. Paradisanos, Interlayer exciton mediated second harmonic generation in bilayer MoS_2, Nat. Commun. **12**, 6894 (2021).

[42] A. M. Jones, H. Yu, J. S. Ross, P. Klement, N. J. Ghimire, J. Yan, D. G. Mandrus, W. Yao, and X. Xu, Spin–layer locking effects in optical orientation of exciton spin in bilayer WSe_2, Nat. Phys. **10**, 130 (2014).

[43] L. Wang, Z. Wang, H. Y. Wang, G. Grinblat, Y. L. Huang, D. Wang, X. H. Ye, X. B. Li, Q. Bao, A. S. Wee, S. A. Maier, Q. D. Chen, M. L. Zhong, C. W. Qiu, and H. B. Sun, Slow cooling and efficient extraction of C-exciton hot carriers in MoS_2 monolayer, Nat. Commun. **8**, 1 (2017).

[44] G. Wang, A. Chernikov, M. M. Glazov, T. F. Heinz, X. Marie, T. Amand, and B. Urbaszek, Colloquium: Excitons in atomically thin transition metal dichalcogenides, Rev. Mod. Phys. **90**, 021001 (2018).

[45] D. Y. Qiu, F. H. da Jornada, and S. G. Louie, Optical spectrum of MoS_2: Many-body effects and diversity of exciton states, Phys. Rev. Lett. **111**, 216805 (2013).

[46] T. Chu, H. Ilatikhameneh, G. Klimeck, R. Rahman, and Z. Chen, Electrically tunable bandgaps in bilayer MoS_2, Nano Lett. **15**, 8000 (2015).

[47] A. Ramasubramaniam, D. Naveh, and E. Towe, Tunable band gaps in bilayer transition-metal dichalcogenides, Phys. Rev. B **84**, 205325 (2011).

[48] N. Zibouche, P. Philipsen, T. Heine, and A. Kuc, Electron transport in MoWSeS monolayers in the presence of an external electric field, Phys. Chem. Chem. Phys. **16**, 11251 (2014).

[49] G. Kresse and J. Furthmüller, Efficient iterative schemes for *ab initio* total-energy calculations using a plane-wave basis set, Phys. Rev. B **54**, 11169 (1996).

[50] J. P. Perdew, K. Burke, and M. Ernzerhof, Generalized gradient approximation made simple, Phys. Rev. Lett. **77**, 3865 (1996).

[51] P. E. Blöchl, Projector augmented-wave method, Phys. Rev. B **50**, 17953 (1994).

[52] R. W. Godby, M. Schlüter, and L. Sham, Accurate exchange-correlation potential for silicon and its discontinuity on addition of an electron, Phys. Rev. Lett. **56**, 2415 (1986).

[53] P. Mori-Sánchez, A. J. Cohen, and W. Yang, Localization and delocalization errors in density functional theory and implications for band-gap prediction, Phys. Rev. Lett. **100**, 146401 (2008).

[54] M. S. Hybertsen and S. G. Louie, Electron correlation in semiconductors and insulators: Band gaps and quasiparticle energies, Phys. Rev. B **34**, 5390 (1986).

[55] X. Gonze, P. Ghosez, and R. Godby, Density-polarization functional theory of the response of a periodic insulating solid to an electric field, Phys. Rev. Lett. **74**, 4035 (1995).

[56] See Supplemental Material at http://link.aps.org/supplemental/10.1103/PhysRevB.109.075417 for the method of second-order susceptibility calculation; details of our implemented scissor correction; details of vacuum spacing and electric field range to prevent electron splitting; electric field effect on ML TMDCs properties: atomic structure, band structure, electrostatic potential energy, band-energy splitting; confirmation of symmetry relationship between second-order susceptibility tensor components; the imaginary part of dielectric function and joint density of states for ML TMDCs; similar analysis for other ML TMDCs which do not appear in the main text. It also contains Refs. [57–62].

[57] H. H. Gürel, V. O. Özçelik, and S. Ciraci, Effects of charging and perpendicular electric field on the properties of silicene and germanene, J. Phys.: Condens. Matter **25**, 305007 (2013).

[58] X.-P. Wang, X.-B. Li, N.-K. Chen, J.-H. Zhao, Q.-D. Chen, and H.-B. Sun, Electric field analyses on monolayer semiconductors: The example of InSe, Phys. Chem. Chem. Phys. **20**, 6945 (2018).

[59] C. T. Le, D. J. Clark, F. Ullah, J. I. Jang, V. Senthilkumar, Y. Sim, M. J. Seong, K. H. Chung, J. W. Kim, S. Park, S. H. Rhim, G. Kim, and Y. S. Kim, Impact of selenium doping on resonant second-harmonic generation in monolayer MoS_2, ACS Photonics **4**, 38 (2017).

[60] L. M. Malard, T. V. Alencar, A. P. M. Barboza, K. F. Mak, and A. M. De Paula, Observation of intense second harmonic generation from MoS_2 atomic crystals, Phys. Rev. B **87**, 201401(R) (2013).

[61] Y. Li, Y. Rao, K. F. Mak, Y. You, S. Wang, C. R. Dean, and T. F. Heinz, Probing symmetry properties of few-layer MoS_2 and h-BN by optical second-harmonic generation, Nano Lett. **13**, 3329 (2013).

[62] G. Wang, X. Marie, I. Gerber, T. Amand, D. Lagarde, L. Bouet, M. Vidal, A. Balocchi, and B. Urbaszek, Giant enhancement of the optical second-harmonic emission of WSe_2 monolayers by laser excitation at exciton resonances, Phys. Rev. Lett. **114**, 097403 (2015).

[63] J. Sun, Y. Gu, D. Y. Lei, S. P. Lau, W.-T. Wong, K.-Y. Wong, and H. L.-W. Chan, Mechanistic understanding of excitation-correlated nonlinear optical properties in MoS_2 nanosheets and nanodots: The role of exciton resonance, ACS Photonics **3**, 2434 (2016).

[64] N. A. Pike and R. Pachter, Second-order nonlinear optical properties of monolayer transition-metal dichalcogenides by computational analysis, J. Phys. Chem. C **125**, 11075 (2021).

[65] J. Liang, J. Zhang, Z. Li, H. Hong, J. Wang, Z. Zhang, X. Zhou, R. Qiao, J. Xu, P. Gao, Z. Liu, Z. Liu, Z. Sun, S. Meng, K. Liu, and D. Yu, Monitoring local strain vector in atomic-layered $MoSe_2$ by second-harmonic generation, Nano Lett. **17**, 7539 (2017).

[66] L. Mennel, V. Smejkal, L. Linhart, J. Burgdorfer, F. Libisch, and T. Mueller, Band nesting in two-dimensional crystals: An

exceptionally sensitive probe of strain, Nano Lett. **20**, 4242 (2020).

[67] D. Moss, E. Ghahramani, J. Sipe, and H. Van Driel, Band-structure calculation of dispersion and anisotropy in $\chi \rightarrow^{(3)}$ for third-harmonic generation in Si, Ge, and GaAs, Phys. Rev. B **41**, 1542 (1990).

[68] G. Guo, K. Chu, D. Wang, and C. Duan, Linear and nonlinear optical properties of carbon nanotubes from first-principles calculations, Phys. Rev. B **69**, 205416 (2004).

[69] C. Duan, J. Li, Z. Gu, and D. Wang, First-principles calculation of the second-harmonic-generation coefficients of borate crystals, Phys. Rev. B **60**, 9435 (1999).

[70] J. L. Hughes and J. Sipe, Calculation of second-order optical response in semiconductors, Phys. Rev. B **53**, 10751 (1996).

[71] J. Sipe and E. Ghahramani, Nonlinear optical response of semiconductors in the independent-particle approximation, Phys. Rev. B **48**, 11705 (1993).

[72] E. Ghahramani, D. Moss, and J. Sipe, Second-harmonic generation in odd-period, strained, $(Si)_n$ $(Ge)_n$/Si superlattices and at Si/Ge interfaces, Phys. Rev. Lett. **64**, 2815 (1990).